ADVANCED MATERIALS TECHNOLOGIES
www.advmattechnol.de

Circularly Polarized Light Detection Through 3D Chiral Metasurface-Based Phototransistors

Saravanan Rajamani, Daniela Simeone, Alessandro Pecora, Mariachiara Manoccio, Gianluca Balestra, Ayaz H. Bayramov, Nazim T. Mamedov, Adriana Passaseo, Giuseppe Gigli, David Maria Tobaldi, Vittorianna Tasco, Marco Esposito, Adriano Cola, and Massimo Cuscunà**

Distinguishing between different handedness of circularly polarized light can be a useful additional property in photodetector technology. The integration of this functionality can be obtained either using optical media with chiro-optical response, or by the employment of chiral metamaterials. In this work, 3D chiral metasurfaces composed by a 3D helix array, are integrated onto a micrometer-scale silicon-based transistor and act as optical filter for circularly polarized light. The technological process involving focused electron beam induced deposition for helix manufacturing is carefully studied with respect to its effect on the phototransistor response. The integrated system exhibits a photoresponse which is dependent on the circular polarization, with a promising asymmetry factor in the visible spectral range. The proposed technology can pave the way for novel potential applications in diverse areas such as materials science, bioimaging, and quantum computing.

1. Introduction

Circularly polarized light (CPL) is a polarized light in which the electric field has constant magnitude but its vector continuously rotates in a plane (i.e., right-handed or left-handed circular polarization, respectively RCP and LCP) with a steady rate.[1,2] In recent years, CPL detection has unlocked potential applications for a wide range of areas such as optical communication of spin information,[3,4] magnetic recording,[5–8] ellipsometric tomography,[9] remote sensing,[10,11] optical information processing,[12,13] and advanced biosensing.[14,15] Traditionally, CPL is detected by using achiral photodetectors and conventional bulky optics, namely, quarter waveplates ($\lambda/4$) and linear polarizers. Given recent trends in miniaturization, the use of devices comprising absorbing materials, such as chiral organic compounds or chiral perovskites,[16] is emerging. These materials are intrinsically chiral, and have the potential to differentiate between RCP and LCP light.[17–25] Another direction involves the integration of chiral metamaterials with conventional semiconductor technologies for photodetection.[26] In a pioneering work

S. Rajamani, D. Simeone, M. Manoccio, G. Balestra, A. Passaseo, G. Gigli, D. M. Tobaldi, V. Tasco, M. Esposito, M. Cuscunà
CNR Nanotec
Institute of Nanotechnology
University Campus Ecotekne
Via per Monteroni, Lecce 73100, Italy
E-mail: vittorianna.tasco@nanotec.cnr.it; massimo.cuscuna@nanotec.cnr.it

The ORCID identification number(s) for the author(s) of this article can be found under https://doi.org/10.1002/admt.202301250

Tasco is currently seconded at the European Research Council Executive Agency of the European Commission. Her views expressed in this paper are purely those of the writer, may not in any circumstance be regarded as stating an official position of the European Commission.

DOI: 10.1002/admt.202301250

A. Pecora
CNR IMM
Institute for Microelectronics and Microsystems
Via del Fosso del Cavaliere 100, Roma 00133, Italy

G. Balestra, G. Gigli
Department of Mathematics and Physics "Ennio De Giorgi"
University of Salento
C/o Campus Ecotekne, Via per Monteroni, Lecce 73100, Italy

A. H. Bayramov, N. T. Mamedov
Ministry of Science and Education
Institute of Physics
131 Javid ave., Baku Az1143, Azerbaijan

N. T. Mamedov
Baku State University
33 Z.Khalilov str., Baku Az1148, Azerbaijan

A. Cola
CNR IMM
Institute for Microelectronics and Microsystems
University Campus Ecotekne
Via per Monteroni, Lecce 73100, Italy

demonstrating a hot electron-based CPL-detecting diode,[20] an n-type silicon wafer has been put in contact with chiral plasmonic nanostructures (Z-shape Ag metasurfaces). These nanostructures absorb photons, generating high energy electrons within the metal, which can emit over the Schottky interface, leading to a detectable current.[20] The device exhibited asymmetric photoresponsivity, with a difference of 1.5 mA W^{-1} at the resonance, peaked in the NIR spectral region.

Most recently, Namgung et al.[27] exploited an InGaZnO (IGZO) transistor to capture hot electrons with larger and significantly asymmetric responsivity in the visible: 6.5 and 3.62 A W^{-1} at a gate voltage of 20 V under 780 nm LCP and RCP light illumination, respectively. Li et al.[26] reported the integration of a set of chiral plasmonic metasurfaces with a graphene–silicon photodetector for effective full-Stokes polarimetry in the NIR. A CPL detector was also demonstrated by integrating a geometry-controlled TiO_2–SnO_2 hetero-chiral thin film on a Si-based photodetector,[28] or by the insertion of X-shaped Al-Al_2O_3-Al sandwich structures on the top of a metal-semiconductor photodetector.[21] Therefore, the integration of chiral plasmonic nanostructures with semiconductor devices appears to be an extremely promising route for efficient CPL detection.

In the aforementioned experiments, the chiral nanostructures were fabricated using multi-step lithographic approaches combined with the thermal evaporation of metals. By using focused ion/electron beam induced deposition, we have demonstrated that chiral nanostructures can be realized also in a single process run without lithographic steps, with a fully 3D helix shape. As a result of light-handedness dependent excitation of electric dipoles along the single helix wire,[29] arrays of these nanostructures grown on ITO substrates have shown large asymmetric response when interacting with visible CPL in passive transmission schemes.

To explore their potential in active photonic circuits, here we propose their direct integration on the active area of a silicon-based, high responsivity phototransistor (PT). As the CPL incident on the device will be filtered by the chiral metacrystal and then absorbed by the underlying phototransistor, different photocurrent is expected to be generated.[21] From a technological perspective, the proposed approach presents a twofold set of advantages. On one hand, the PT technology, consisting of a photosensitive semiconductor, combines light detection and signal amplification in a single device.[30] On the other hand, focused electron beam induced deposition (FEBID) and focused ion beam induced deposition (FIBID) provide a high degree of freedom in the design, the ability to realize core/shell and composite structures, and high spatial resolution in a single writing step.[31–33] However, the high energy of the beams when combined with the PT, may pose nontrivial limitations on the exploitation of this approach, potentially impacting the electrical transfer characteristics, an aspect that we will explore in the present study.

2. Experimental Section

2.1. Amorphous Silicon Thin Film Transistor Fabrication

We have fabricated a common back gate a-Si:H inverted staggered TFT structure on p-type Si (100) wafer (thickness ≈400 µm) with a low resistivity < 0.005 Ohm × cm (high doped substrates) with a thermal oxide layer on top (100 nm) working as gate dielectric. A 80 nm-thick undoped a-Si:H layer acts as the semiconductor active material, whereas a 20 nm-thick, highly phosphorous doped (n^+) a-Si layer was patterned by optical lithography to realize ohmic source and drain contacts. The fabrication steps of the a-Si:H TFT are shown in **Figure 1**. In detail, undoped hydrogenated a-Si was first deposited by using RF-plasma enhanced chemical vapour deposition (RF-PECVD) on the Si-wafer with thermal oxide, at a substrate temperature of 250°C. Then, the n^+ doped a-Si:H layer was sequentially deposited.

Deposition conditions were:

i. a-Si:H, 20 sccm SiH_4, T_s = 250 °C, P_{RF} = 20 mW cm^{-2}, and p = 0.3 Torr;
ii. n^+ a-Si:H, 20 sccm of 1% PH_3 in SiH_4, T_s = 250 °C, P_{RF} = 20 mW cm^{-2} and p = 0.3 Torr.

Ohmic source-drain contacts were formed removing n^+ from the channel region by using photolithographic patterning and RF-Reactive Ion Etching (RIE) in O_2 (25%) and CF_4 (50%) gas mixture at p = 500 mTorr (Figure 1). Then, a second photolithographic step was applied followed by a second RIE step to define the device islands. Finally, a 150 nm thick Al—Si metal layer was thermally evaporated followed by the third photolithographic step to form source-drain metal contacts. The TFTs were realized with an a-Si:H active area of ≈10 × 10 µm^2.

2.2. Helix Array Growth by FEBID

Substrates with fabricated a-Si:H TFTs were cleaned with acetone and isopropanol and loaded in a dual configuration focused ion beam (FIB)/SEM system, a Carl Zeiss Auriga40 Crossbeam, equipped with the Cobra FIB column and a gas injection system (GIS) with five gas channels. For FEBID nanohelices, we employed trimethyl(methylcyclopentadienyl)-platinum(IV) [$(CH_3)_3(CH_3C_5H_4)Pt$] as metalorganic precursor, locally injected through the nozzle at the upper side of the sample. The nanohelices were grown one by one through an electron beam scanning direction perpendicular to the precursor gas flow. We optimized the injection distance between the substrate and the nozzle to obtain high growth control by a suitable gas density. The single loop nanohelices were grown at an electron beam current of 50 pA, an accelerating voltage of 10 or 2 keV, respectively, a step size of 2 nm, and a dwell time of 8 ms. In the case of 2 loop helices, the second loop was realized with a dwell time of 16 ms to compensate the 3D proximity effect.[34] The chamber pressure was stable at 1 × 10^{-5} mbar during the deposition time. The Raith elphy multibeam pattern generator controlled exposure parameters of the electron beam. The base pattern layout consists of an empty circle that is scanned one or two times by the electron beam to create 1 or 2 loop nanohelices, respectively.

2.3. Monte–Carlo Simulations

The electron interaction with active layers of TFTs was modelled with a Monte–Carlo simulation by using the CASINO software.[35,36] CASINO is a Monte–Carlo simulation tool designed for modeling electron trajectory in solids. It is specially designed for low beam interaction in bulk materials and thin films.

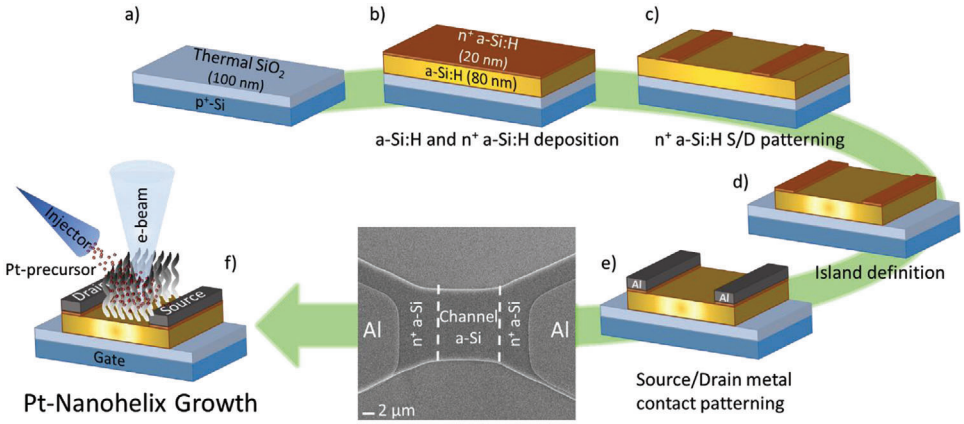

Figure 1. Fabrication process sketch of the circularly polarized light detector with 3D chiral helices integrated on a hydrogenated amorphous silicon thin film transistor. a) Thermal SiO_2 is first deposited, b) a sequential deposition of undoped and doped a:Si-H films is performed, c) patterning of the doped a:Si-H source and drain contacts, d) island definition to electrically separate the various devices, e) definition of source/drain metal contact. The scanning electron microscopy (SEM) micrograph presents a top view of the final architecture of the a-Si:H-based TFT, with an active area of $10 \times 10\ \mu m^2$ located between the doped a:Si-H source/drain contacts. f) The nanohelices array is finally deposited on the active area using focused electron beam induced deposition in combination with Pt metalorganic precursor.

We utilized 20 000 electrons for trajectory simulation at both 2 and 10 keV energies of the primary beam.

The mass densities used for a-Si:H and thermal SiO_2 are 2.3[37,38] and 2.21 g cm^{-3},[37] respectively.

2.4. Electrical and Electro-Optical Characterization

The TFT electrical characterizations were carried out in a K. Suss probe station by using an Agilent B1500A semiconductor device parameter analyzer. For evaluating the response to circularly polarized light of transistors, equipped with the 3D chiral metamaterial, a spectral photocurrent set-up was adapted. The monochromatized light of a tungsten lamp was sent, by means of an optical fiber, to a lens tube assembly able to zoom and collimate the optical beam. A linear polarizer and a quarter-wave plate were properly positioned above the sample to ensure the Right and Left circular light polarization. A circular spot of ≈0.8 mm was incident on the sample. The measurements were performed with light under normal incidence to the substrate containing the helix arrays. Photocurrent was measured under a continuous beam by using a pA-meter.

3. Results and Discussion

We started from the fabrication of hydrogenated amorphous-Si (a-Si:H) thin film transistors (TFTs),[39–41] and then compact arrays of nanohelices were realized on the active area of the devices by focused ion/electron beam induced deposition. The fabrication scheme is shown in Figure 1 (for details see the Experimental Section).

The a-Si:H exhibits a direct band gap in the range 1.5–2.0 eV depending on growth conditions and hydrogen content.[42–45] The amorphous nature of the material makes it able to absorb visible light effectively. The growth of a-Si:H films is typically carried out by using a plasma deposition process that is suitable for large-scale production as it operates at temperatures below 300 °C.[42,46]

Nevertheless, the material contains defects like dangling, strained, and weak bonds, which diminish its efficiency by serving as recombination sites for both electrons and holes. These defects originate from the band tails and hinder the flow of charge carriers. To reduce the density of these defects, hydrogen is introduced into the material, creating an alloy of amorphous silicon and hydrogen, commonly referred to as hydrogenated amorphous silicon, which enhances photon absorption efficiency. Hydrogenated amorphous silicon has also disadvantages due to its structure; in particular, a prolonged exposure to light, as occurs in amorphous silicon solar cells, leads to an increase in the density of states in the energy gap due to the Staebler–Wronski effect.[47] This increase in the density of states is due to the formation of silicon dangling bonds. Despite the light-induced degradation of amorphous silicon, the latter is frequently used for realizing phototransistors,[48] because of a high ratio of photocurrent to dark current and a good saturation in the output photocurrent. Therefore, in the present work we used a simplified TFT design based on a highly photosensitive semiconductor, as a-Si:H is, to demonstrate the ability of a miniaturized device equipped with 3D chiral helices to discriminate RCP and LCP incident light.

The integration of the chiral medium is carried out on the sensitive area of the phototransistor (of the order of $10 \times 10\ \mu m$). To create arrays of nanohelices with a proper control over size and spatial arrangement, both focused ion and electron beam can be used. In particular, the employment of a gallium ion beam can enhance the range of achievable material combinations.[31–33] When combined with a Pt-precursor, the Ga-ion beam typically results in the incorporation of 50% of metal within the winding nanowire, leading to pronounced plasmonic effects. However, when writing with the Ga-ion beam on the surface of an a-Si:H TFT, some damage effects have been observed, as discussed in detail in the supplementary materials (Figure S1, Supporting Information).

On the other hand, a FEBID approach,[32] as shown below through simulations and experimental results, does not induce detrimental changes in the electrical transfer characteristics.

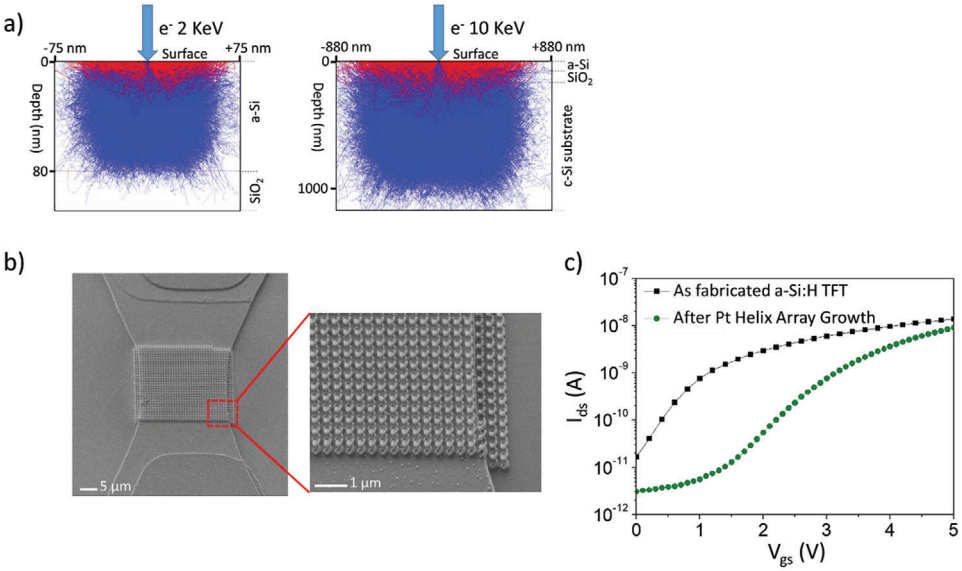

Figure 2. a) Calculated penetration depth by irradiating the sample with an electron beam energy of 2 keV (left panel), and 10 keV (right panel); a large number of electrons (20 000) was set to better evaluate the penetration depth in the TFT heterostructure. b) SEM images (3D view) of an amorphous silicon-based TFT with a 1 loop Pt/C mix-based nanohelix array (lateral pitch = 350 nm, vertical pitch = 450 nm, wire diameter = 50 nm, external diameter = 220 nm, one full revolution), fabricated on top of the TFT active region by a FEBID approach at an electron beam energy of 2 keV. c) Dark transfer characteristics (I_{ds}-V_{gs}, semi-logarithmic scale), measured at V_{ds} 0.5 V, of the a-Si:H TFT reported in panel b), before (black symbols) and after (green symbols) helix growth.

Figure 2a analyzes, through Monte Carlo simulations the interaction of a focused electron beam with the transistor heterostructure (details on the model can be found in the Experimental Section). As expected, the higher the energy, the longer the beam penetration depth. In the case of 10 keV (Figure 2a, right panel), the electron trajectories cross the silicon/silicon oxide interface, reaching the c-Si substrate with a penetration depth of ≈1 µm. Therefore, the prolonged exposure of a-Si:H to 10 keV electron beam required for the array writing, has the potential to generate a large amount of interface trap states and defects in a-Si:H through an electronic excitation of the Si–H and Si–Si resulting in breaking of weaker bonds and subsequently end up as dangling bonds. As expected, the relative TFT transfer electrical characteristic (source-drain current vs gate-to-source voltage, I_{ds}–V_{gs}), after the nanohelix growth, reported the absence of source-drain current modulation induced by gate polarization (Figure S2, Supporting Information). In contrast, an electron beam energy of 2 keV restricts the depth to which the electrons can penetrate the sample (as shown in the left panel of Figure 2a) and reduces the amount of damage to the a-Si:H semiconductor. This observation suggests that the growth of 3D helical-shaped nanostructures with high precision using a low energy electron beam can minimize the negative impact on the underlying device's electrical transfer characteristics.

Figure 2b reports the scanning electron microscopy image of the amorphous silicon-based TFT with an array of nanohelices on top of the active region (10×10 µm^2). The helices are obtained using the FEBID approach, with an electron beam energy of 2 keV, in combination with Pt-precursor. The employed beam and pattern growth conditions provided a uniform nanohelix array with a lateral pitch of 350 nm. Each helix exhibits a wire diameter (WD) of 50 nm, an external diameter (ED) of 220 nm, and a full revolution vertical pitch (VP) of 450 nm, while the composition is expected to be a combination of Pt and C.[32]

Electrical measurements were conducted to better analyze the TFT properties before and after nanohelix array growth (Figure 2c). As can be noted, before fabricating helices, the electrical transfer characteristic (measured at drain-to-source voltage, $V_{ds} = 0.5$ V) was featured by a subthreshold slope of about 0.4 V per decade and a threshold voltage (V_{th}) of about 1.5 V, while the retrieved field effect mobility electron was around 0.7 cm^2 Vs^{-1}. After FEBID process, the TFT undergoes a positive threshold voltage shift ($+\Delta V_{th}$) of ≈2 V (V_{th} = 3.5 V) (Figure 2c). Such effect is likely related to acceptor-type defects formation near the valence band edge at the a-Si:H/SiO_2 interface, which induces an increase in the hole density in the valence band of the amorphous silicon with a consequent positive shift of the V_{th}, as already observed for n-type TFTs irradiated with an electron beam.[49] Actually, the mentioned defect formation at the amorphous silicon/silicon oxide interface is supported by Monte–Carlo simulations (Figure 2a, left panel), that clearly highlight electron trajectories reaching such an interface.

It is worth noting that the increase in the threshold voltage is also due to a subthreshold slope increase up to 0.7 V per decade. The latter originates from the formation of localized electronic states, occurring in the bandgap of the amorphous silicon (deep states mostly consisting of Si dangling bonds), due to the electron beam irradiation during the nanohelix growth. This damage caused by the low energy electron beam is similar to the light-induced degradation previously mentioned, Staebler–Wronski effect,[47] and resulting in the degradation of the optoelectronic properties of a-Si:H films. Despite such a slight degradation, the low accelerating voltage induced deposition process required for the proper formation of Pt-based helices, induces minimal

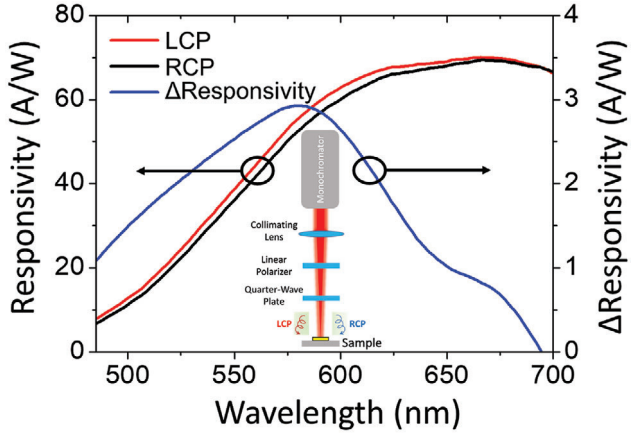

Figure 3. Responsivity of an amorphous silicon-based TFT equipped with a 1 loop Pt/C mix-nanohelix array upon exposure to left-handed and right-handed circularly polarized illumination. The TFT was biased in the off-regime (gate voltage V_{gs} = 1.5 V, V_{gs}–V_{th} = −2 V and drain voltage V_{ds} = 2 V). The difference between the responsivities (ΔResponsivity) induced by LCP and RCP light irradiation is also reported, a maximum value of 3 A W^{-1} was achieved. The inset reports the sketch of the optical setup used to produce left-handed and right-handed circularly polarized illumination.

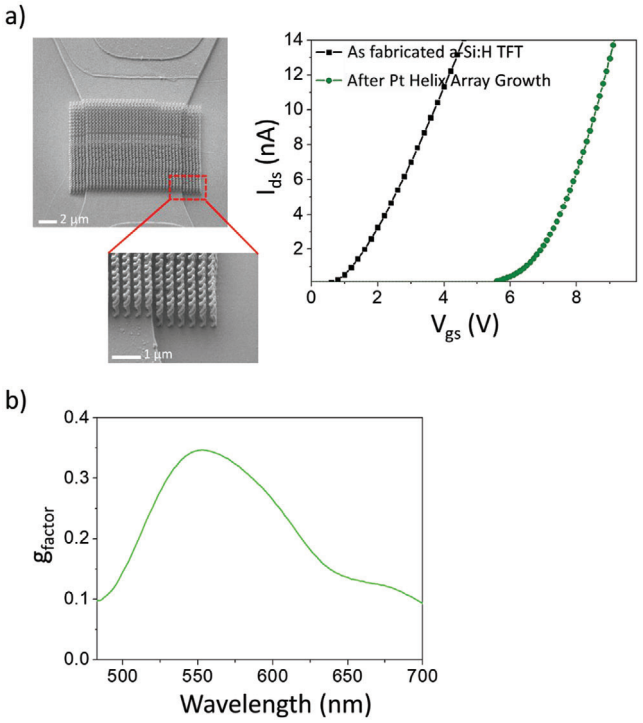

Figure 4. a) SEM images of two loop Pt/C mix-helix array fabricated on a-Si:H TFT active region (10 × 10 μm^2) (left panel), I_{ds}–V_{gs} characteristics (linear scale) before and after helix growth, measured at V_{ds} 0.5 V (right panel). b) g_{factor} value calculated by the measured RCP and LCP photocurrents, I_{ph} (LCP) and I_{ph} (RCP) reported in Figure S4a (Supporting Information).

damage to the channel region and the TFTs correctly switch between the off and on states.

The CPL, generated from a lamp through a linear polarizer and a quarter-wave plate, was focused on the sample as shown in the inset of **Figure 3**. The input wavelength was swept from 480 to 700 nm, and the transistor was biased in the off-regime (V_{gs}–V_{th} = −2 V and drain voltage V_{ds} = 2 V). That bias in the off-regime allows the maximization of the ratio between the photocurrent and the dark current compared to the on-regime, where the dark current magnitude becomes comparable with the photocurrent, as displayed in Figure S3 (Supporting Information). Hence, it is evident that the off-regime represents the most favorable configuration to detect the tiny changes induced by the different light polarizations.

In the investigated spectral range, the responsivity achieved under LCP illumination is slightly higher than the RCP one (Figure 3), demonstrating a selection ability between RCP and LCP light. It is worth noting that the TFT dark current was subtracted to the measured photocurrents. The difference between the responsivities generated under RCP and LCP irradiation is also shown in Figure 3. The figure demonstrates better spectrally selective dichroic filtering in the middle of the visible region, with a value ≈3 A W^{-1}, and a null difference ≈700 nm. As demonstrated in our previous works,[31–33] for right-handed Pt/C mix-helix structures, right-handed circularly polarized light is strongly absorbed due to the matching between RCP light and helix twist. This allows mostly LCP light to reach the a-Si:H active layer, and generate a larger photocurrent. It is worth noting that the responsivities observed with RCP and LCP light in Figure 3 are strongly driven by that of the bare TFT (without helix growth) shown in Figure S3b (Supporting Information).

Such encouraging results have motivated us to attempt to further improve the device performance. Therefore, we explored the integration of a similar array grown under the same conditions but with double loop helices (**Figure 4**a, left panel). Electrical measurements were conducted to better analyze the TFT properties also before and after the double loop nanohelix array growth. As it can be noted, before fabricating helices, the transfer electrical characteristic (measured at V_{ds} 0.5 V) was featured by a low threshold voltage of ≈1.8 V. Conversely, after the helix integration by FEBID, the electrical characteristic undergoes a threshold voltage shift of ≈5.2 V (V_{th} = 7 V), as depicted in Figure 4a (right panel). Actually, the prolonged exposure of a-Si:H to 2 keV electron beam for growing a double loop helix array has the potential to generate a huge number of acceptor-type defects at the a-Si:H/SiO_2 interface, with a consequent larger positive shift of the V_{th} as compared to the single loop case.

The spectral response of the TFT equipped with the double loop Pt/C-helical array was recorded in the range 480–700 nm. Similarly, to the case of a single loop helix array, the TFT was biased in the off-regime (V_{gs}–V_{th} = −2 V). The photocurrents induced by LCP and RCP incident light are reported in Figure S4a (Supporting Information). The latter reports a selective dichroic filtering in a larger spectral range with respect to single loop case. Actually, the null point in the difference between the LCP and RCP light excitation induced-photocurrents red-shifted toward values larger than 700 nm (Figure S4b, Supporting Information). Such an enlargement in the dichroic band by increasing the number of helix loops was already observed and deeply discussed in our previous works.[33] In order to better compare the efficiency

of the fabricated devices with double and single loop helices, we calculated the anisotropy factor (g) (Figure 4b) defined as:

$$g = 2\frac{I_{ph}(LCP) - I_{ph}(RCP)}{I_{ph}(LCP) + I_{ph}(RCP)} \quad (1)$$

Notice that this factor provides a way to normalize the difference between the photocurrents, generated by RCP and LCP light, to the total photocurrent, making it more suitable for comparison purposes.[32] With double loop helices, the light absorption of the chiral array increases considerably, and this is expected to improve the polarization discrimination. Consistently, the anisotropy factor observed in the TFT structure equipped with the double loop Pt-helical nanostructure array, ≈0.35 at 560 nm (see Figure 4b), was larger than what was observed in the single-loop helix array, where the highest value was ≈0.17 at 490 nm. The g_{factor} value could be further enhanced by additional device optimization. Actually, in the case of Pt precursor dissociated by the focused electron beam, we know that a lower metal percentage is contained in the winding wire,[32] leading to a less pronounced plasmonic behavior, as compared to what obtained with the ion beam. The latter could be used in the next PT architecture by introducing a sacrificial SiO_2 thick layer on the a-Si:H one, capable of stopping ions before they penetrate to the semiconductor.

We conclude the discussion of TFT photoelectric properties with a brief mention of reliability, optical excitation power and time response. Before employing a monochromatized tungsten lamp, we conducted several measurements under much higher optical densities (≈10 mW) by using laser excitation at 660 nm. Despite the higher photocurrent values, the spectral response and transfer characteristics were found to be influenced by incident optical density, with significant degradation observed during prolonged exposures. As mentioned above, this behavior is typical of a-Si:H and is associated with light-induced defects.[47] Given our focus on the polarization discrimination capability of helical arrays, we adopted measurement conditions to minimize these detrimental effects and ensure reliable results. Several devices were tested at low optical excitation levels, demonstrating a good level of reproducibility. An average maximum g_{factor} was estimated to be ≈0.35 ± 0.02. For what concerns the response time, this is a general figure-of-merit characterizing the performance of photodetectors. For a-Si:H based phototransistors, typical values have been reported in the range of tens to hundreds of μs,[50,51] with multi-trapping being the limiting mechanism.[51] As the helix structure only affects the light absorption mechanism, we do not expect the time response of our devices to significantly differ from their TFT analogues.

The calculated g_{factor} was also compared to the one measured on a Pt/C mix-helix array fabricated by FEBID at 2 keV on an indium tin oxide (ITO) substrate, with identical structural features and fabrication tolerance. In that case, we used a conventional optical setup composed by an optical microscope and a camera for collecting CPL light, as described in previous works.[31–34] As can be noted in Figure S5a (Supporting Information), at energy as low as 2 keV, the density of the generated SEs leads to the appearance of a secondary helix structure as already reported for nanohelices realized on the TFT active area at similar energy (Figure 4a, left panel). Figure S5b (Supporting Information) (right panel) shows the g_{factor} calculated by the measured RCP and LCP optical transmissions (Figure S5b, Supporting Information, left panel), as follows:

$$g = 2\frac{T_{LCP} - T_{RCP}}{T_{LCP} - T_{RCP}} \quad (2)$$

A maximum value of g at 540 nm was observed, in good agreement with the results achieved by means of a double loop Pt/C-helix array integrated on the TFT active area (Figure 4b). Finally, from results in Figure 4 and Figure S4 (Supporting Information), we demonstrated the ability of the proposed TFT architecture to discriminate RCP and LCP incident light within an integrated and miniaturized system, and without bulky optics.

4. Conclusion

In conclusion, we have presented an integrated and miniaturized chiral photodetector, where the response of a phototransistor based on amorphous silicon becomes selective to the handedness of circular polarized light in the visible spectral range. Such a functionality was enabled by a 3D chiral metasurface consisting of ordered array of nanohelices, prototyped by focused electron beam induced deposition, and exhibiting chiro-optical behavior in such a range. Further improvement can be envisaged by considering different combinations of nanohelix materials with improved circular polarization selectivity, and phototransistor materials with better resistance to high energy beam damage.

Supporting Information

Supporting Information is available from the Wiley Online Library or from the author.

Acknowledgements

The work was supported by the Italian Ministry of Research, under the complementary actions to the National Recovery and Resilience Plan (co-financed by the Next Generation EU): "NFFA-DI – Nano Foundries and Fine Analysis – Digital Infrastructure" Grant (Code: IR0000015, CUP: B53C22004310006), and "Fit4MedRob – Fit for Medical Robotics" Grant (#PNC0000007), the "Tecnopolo per la Medicina di Precisione" (TecnoMed Puglia) – Regione Puglia: DGR no. 2117 del 21/11/2018 CUP: B84I18000540002, the International cooperation project "Hybrid 3D Chiral Metamaterial/2D MoS2 Phototransistors for Circularly Polarized Light Detection" (HYSPID), CUP: B86C18000430006, funded by the Italian National Research Council and the Ministry of Science and Education of Azerbaijan (Institute of Physics), and the Regional (Puglia) project Innonetwork "IN-AIR", CUP: B37H17004840007. The authors are very much obliged to Ms Iolena Tarantini (University of Salento) and Mr Gianmichele Epifani (CNR NANOTEC) for technical support. The authors thank Dr Elvin H. Alizade (Ministry of Science and Education of Azerbaijan, Institute of Physics) for scientific discussion. Dr Francesco Gabellone (CNR NANOTEC) is kindly acknowledged for his help in the graphical editing.

Conflict of Interest

There are no conflicts to declare.

Data Availability Statement

The data that support the findings of this study are available from the corresponding author upon reasonable request.

Keywords

3D chiral metasurfaces, circular polarized light detection, focused electron beam induced deposition, handedness-selectivity, nanohelices, phototransistors

Received: October 16, 2023
Revised: November 28, 2023
Published online: December 24, 2023

[1] S. Huard, *Polarization of Light*, John Wiley, Masson, Chichester; New York, Paris **1997**.
[2] (Eds.: N. Berova, K. Nakanishi, R. Woody), *Circular Dichroism: Principles and Applications*, Wiley-VCH, New York, **2000**.
[3] R. Farshchi, M. Ramsteiner, J. Herfort, A. Tahraoui, H. T. Grahn, *Appl. Phys. Lett.* **2011**, *98*, 162508.
[4] S. D. Ganichev, W. Prettl, *J. Phys.: Condens. Matter* **2003**, *15*, R935.
[5] C. D. Stanciu, F. Hansteen, A. V. Kimel, A. Kirilyuk, A. Tsukamoto, A. Itoh, T. h. Rasing, *Phys. Rev. Lett.* **2007**, *99*, 047601.
[6] S. Mangin, M. Gottwald, C.-H. Lambert, D. Steil, V. Uhlíř, L. Pang, M. Hehn, S. Alebrand, M. Cinchetti, G. Malinowski, Y. Fainman, M. Aeschlimann, E. E. Fullerton, *Nature Mater* **2014**, *13*, 286.
[7] K. H. Nordsieck, K. P. Jaehnig, E. B. Burgh, H. A. Kobulnicky, J. W. Percival, M. P. Smith, in Polarimetry in Astronomy, SPIE, **2003**, pp. 170.
[8] C. Pernechele, E. Giro, D. Fantinel, in Polarimetry in Astronomy, SPIE, **2003**, pp. 156.
[9] C.-M. Jan, Y.-H. Lee, K.-C. Wu, C.-K. Lee, *Opt. Express* **2011**, *19*, 5431.
[10] D. A. Talmage, P. J. Curran, *Int. J. Remote Sensing* **1986**, *7*, 47.
[11] J. Luo, D. Liu, Z. Huang, B. Wang, J. Bai, Z. Cheng, Y. Zhang, P. Tang, L. Yang, L. Su, *Appl. Opt.* **2017**, *56*, 6837.
[12] J. F. Sherson, H. Krauter, R. K. Olsson, B. Julsgaard, K. Hammerer, I. Cirac, E. S. Polzik, *Nature* **2006**, *443*, 557.
[13] C. Wagenknecht, C.-M. Li, A. Reingruber, X.-H. Bao, A. Goebel, Y.-A. Chen, Q. Zhang, K. Chen, J.-W. Pan, *Nature Photon* **2010**, *4*, 549.
[14] M. Manoccio, V. Tasco, F. Todisco, A. Passaseo, M. Cuscuna, I. Tarantini, G. Gigli, M. Esposito, *Adv. Sci.* **2023**, *10*, 2206930.
[15] M. Manoccio, M. Esposito, E. Primiceri, A. Leo, V. Tasco, M. Cuscunà, D. Zuev, Y. Sun, G. Maruccio, A. Romano, A. Quattrini, G. Gigli, A. Passaseo, *Nano Lett.* **2021**, *21*, 6179.
[16] X. Shang, L. Wan, L. Wang, F. Gao, H. Li, *J. Mater. Chem. C* **2022**, *10*, 2400.
[17] Y. Yang, R. C. Da Costa, M. J. Fuchter, A. J. Campbell, *Nat. Photonics* **2013**, *7*, 634.
[18] W. Xiao, X. Shi, Y. Zhang, W. Peng, Y. Zeng, *Phys. Scr.* **2019**, *94*, 085501.
[19] A. Ishii, T. Miyasaka, *Sci. Adv.* **2020**, *6*, eabd3274.
[20] W. Li, Z. J. Coppens, L. V. Besteiro, W. Wang, A. O. Govorov, J. Valentine, *Nat. Commun.* **2015**, *6*, 8379.
[21] X. Shi, W. Xiao, Q. Fan, T. Zhou, W. Song, C. Zhang, Y. Zeng, W. Peng, *IEEE Sens. J.* **2018**, *18*, 9203.
[22] L. Wang, Y. Xue, M. Cui, Y. Huang, H. Xu, C. Qin, J. Yang, H. Dai, M. Yuan, *Angew. Chem.* **2020**, *132*, 6504.
[23] D. Li, X. Liu, W. Wu, Y. Peng, S. Zhao, L. Li, M. Hong, J. Luo, *Angew. Chem.* **2021**, *133*, 8496.
[24] H. K. Bisoyi, Q. Li, *Acc. Chem. Res.* **2014**, *47*, 3184.
[25] J. Ahn, E. Lee, J. Tan, W. Yang, B. Kim, J. Moon, *Mater. Horiz.* **2017**, *4*, 851.
[26] L. Li, J. Wang, L. Kang, W. Liu, L. Yu, B. Zheng, M. L. Brongersma, D. H. Werner, S. Lan, Y. Shi, Y. Xu, X. Wang, *ACS Nano* **2020**, *14*, 16634.
[27] S. D. Namgung, R. M. Kim, Y.-C. Lim, J. W. Lee, N. H. Cho, H. Kim, J.-S. Huh, H. Rhee, S. Nah, M.-K. Song, J.-Y. Kwon, K. T. Nam, *Nat. Commun.* **2022**, *13*, 5081.
[28] S. H. Lee, D. P. Singh, J. H. Sung, M.-H. Jo, K. C. Kwon, S. Y. Kim, H. W. Jang, J. K. Kim, *Sci. Rep.* **2016**, *6*, 19580.
[29] M. Esposito, M. Manoccio, A. Leo, M. Cuscunà, Y. Sun, E. Ageev, D. Zuev, A. Benedetti, I. Tarantini, A. Passaseo, V. Tasco, *Adv Funct Mater.* **2022**, *32*, 2109258.
[30] S. H. Yuan, Z. Pei, H. C. Lai, P. W. Li, Y. J. Chan, *Org. Electron.* **2015**, *27*, 7.
[31] M. Cuscunà, M. Manoccio, M. Esposito, M. Scuderi, G. Nicotra, I. Tarantini, A. Melcarne, V. Tasco, M. Losurdo, A. Passaseo, *Mater. Horiz.* **2021**, *8*, 187.
[32] M. Esposito, V. Tasco, M. Cuscunà, F. Todisco, A. Benedetti, I. Tarantini, M. D. Giorgi, D. Sanvitto, A. Passaseo, *ACS Photonics* **2015**, *2*, 105.
[33] M. Esposito, V. Tasco, F. Todisco, M. Cuscunà, A. Benedetti, M. Scuderi, G. Nicotra, A. Passaseo, *Nano Lett.* **2016**, *16*, 5823.
[34] M. Esposito, V. Tasco, F. Todisco, A. Benedetti, D. Sanvitto, A. Passaseo, *Adv. Opt. Mater.* **2014**, *2*, 154.
[35] H. Demers, N. Poirier-Demers, A. R. Couture, D. Joly, M. Guilmain, N. de Jonge, D. Drouin, *Scanning* **2011**, *33*, 135.
[36] P. Hovington, D. Drouin, R. Gauvin, *Scanning* **1997**, *19*, 1.
[37] G. S. May, S. M. Sze, *Fundamentals of Semiconductor Fabrication*, Wiley, New York, **2004**.
[38] J. S. Custer, M. O. Thompson, D. C. Jacobson, J. M. Poate, S. Roorda, W. C. Sinke, F. Spaepen, *Appl. Phys. Lett.* **1994**, *64*, 437.
[39] A. Valletta, P. Gaucci, L. Mariucci, A. Pecora, M. Cuscunà, L. Maiolo, G. Fortunato, *J. Appl. Phys.* **2010**, *107*, 074505.
[40] M. Cuscunà, A. Bonfiglietti, R. Carluccio, L. Mariucci, F. Mecarini, A. Pecora, M. Stanizzi, A. Valletta, G. Fortunato, *Solid-State Electron.* **2002**, *46*, 1351.
[41] G. Fortunato, M. Cuscuna, P. Gaucci, L. Maiolo, L. Mariucci, A. Pecora, A. Valletta, F. Templier, *J. Korean Phy. Soc.* **2009**, *54*, 455.
[42] (Ed.: R. A. Street), *Technology and Applications of Amorphous Silicon*, Springer, Berlin, Heidelberg, **2000**.
[43] F. Demichelis, E. Minetti-Mezzetti, A. Tagliaferro, E. Tresso, P. Rava, N. M. Ravindra, *J. Appl. Phys.* **1986**, *59*, 611.
[44] W. Futako, T. Kamiya, C. M. Fortmann, I. Shimizu, *J. Non-Cryst. Solids* **2000**, *266*, 630.
[45] Z. Hafdi, in *Amorphous Silicon Thin-Film Transistors*, Springer International Publishing, Cham, **2023**, pp. 11–21.
[46] A. Shah, J. Meier, A. Buechel, U. Kroll, J. Steinhauser, F. Meillaud, H. Schade, D. Dominé, *Thin Solid Films* **2006**, *502*, 292.
[47] C. R. Wronski, in *Semiconductors and Semimetals* (Ed.:I. Jacques), Elsevier, Amsterdam **1984**, pp. 347–374.
[48] Y. Kaneko, N. Koike, K. Tsutsui, T. Tsukada, *Appl. Phys. Lett.* **1990**, *56*, 650.
[49] H. J. Moon, S. H. Jung, M. K. Ryu, K. I. Cho, E.-J. Yun, B. S. Bae, *J. Korean Physical Society* **2012**, *60*, 254.
[50] B. S. Wu, C.-Y. Chang, Y.-Y. Fang, R. H. Lee, *IEEE Trans. Electron Devices* **1985**, *32*, 2192.
[51] X. Chen, C.-Y. Tai, *Phys. Rev. B* **1989**, *40*, 9652.